Arch. Metall. Mater. **66** (2021), 4, 1163-1170

DOI: 10.24425/amm.2021.136437

ZHIWEI MA[1], SHENG WANG[1*], XUEYAN DU[1], JI ZHANG[1],
RUIFENG ZHAO[1], SHENGQUAN ZHANG[1]

MICROSTRUCTURES AND MICROWAVE-ABSORBING PROPERTIES OF ZnO SMOKE FROM ZINC LEACH RESIDUE TREATED BY CARBOTHERMAL REDUCTION

Much zinc residue is produced during the traditional processes involved in zinc hydrometallurgy in the leaching stage: its composition is complex and valuable metals are difficult to recover therefrom. If not handled properly, it can lead to a waste of resources and environmental pollution. To solve this problem, zinc leach residue specimens were treated using the carbothermal reduction method (CTR) that is easy to operate and has a high energy utilisation rate. The methods, such as X-ray diffraction (XRD), scanning electron microscopy (SEM), transmission electron microscopy (TEM), and scanning transmission electron microscopy (STEM) were used for analytical characterisation. Based on this, this research investigated a structure-function relationship between microstructures and microwave-absorbing properties of ZnO smoke from CTR-treated zinc leach residue. The results demonstrate that microstructures and macro-properties of ZnO smoke obtained at different temperatures differ greatly. Under conditions including a calcination temperature of 1250°C, holding time of 60 min, and addition of 50% and 10% of powdered coal and CaO separately, the ZnO content in the obtained smoke is 99.14%, with regular micron-sized ZnO particles therein. For these particles, the minimum reflection loss (RL_{min}) reached –25.56 dB at a frequency of 15.84 GHz with a matching thickness of 5 mm. Moreover, frequency bandwidth corresponding to $RL < -10$ dB can reach 2.0 GHz. ZnO smoke obtained using this method is found to have excellent microwave-absorbing performance, which provides a new idea for high-value applications of zinc-rich residue.

Keywords: Zinc leach residue, Carbothermal reduction, ZnO smoke, Microwave-absorbing properties

1. Introduction

A large amount of zinc leach residue with complex composition and containing significant amounts of valuable metals is generally produced in hot-acid leaching during zinc hydrometallurgical processing [1-4]. For every 10,000 t of electric zinc produced, about 3000 t of zinc leach residues are generated. The residue is acidic, toxic, and not easily degraded by microorganisms. Its accumulation can pollute the environment and pose a safety hazard [5-7]. How to use the valuable metals found in zinc leach residue has become a focus of much current research. The residue contains a lot of non-ferrous metals and rare metals such as: Pb, Ag, Fe, Cu, In, and Ge, as well as 2% to 8% of Zn.

At present, there are three main methods used to recover and reuse valuable metals in zinc leach residue, *i.e.* pyrometallurgical processing, hydrometallurgical processing, and combinations of the two [8-10]. The high-value utilisation of the residue after extracting valuable metals has become a focus of current research. Among the three methods, when using the pyrometallurgical process to treat zinc leach residue, it is feasible to volatilise selectively the zinc to form a ZnO-rich smoke while retaining other elements in the residue by optimising the process conditions. This is because the saturated vapour pressure of zinc is much greater than that of other elements. In electromagnetic fields, ZnO has a high dielectric constant, endowing it with favourable dielectric loss and semiconductor performance, so it can be used as a high-performance microwave-absorbing material. The carbothermal reduction method (CRM) was used to improve the rate of volatilisation of zinc in zinc leach residue by adjusting process conditions including those relating to the reducing agent, modifier, and reaction temperature. In this way, the relationship between the process conditions and microstructures of ZnO was revealed, laying the foundation for transformation of high value-added materials. The relationships between the standard Gibbs free energy and the temperature in the reduction reaction of zinc compounds from zinc leach residue, and between the saturated vapour pressure and the temperature were determined using FactSage 7.3 software. The feasibility of the

[1] LANZHOU UNIVERSITY OF TECHNOLOGY, STATE KEY LABORATORY OF ADVANCED PROCESSING AND RECYCLING OF NON-FERROUS METALS, LANZHOU 730050, CHINA

* Corresponding author: wangsheng@lut.cn

scheme was demonstrated from the perspectives of thermodynamics (Supplementary materials) and process conditions. According to the CaO-SiO_2-FeO ternary phase diagram plotted using FactSage 7.3, the proportioning process and the range of reaction temperatures were ascertained. The structure-function relationships between microstructures of ZnO smoke and the microwave-absorbing properties, including the electromagnetic parameter, reflection loss (RL), and dielectric loss were revealed by changing the process conditions. In this way, the high-efficiency separation of zinc from other elements in the residue was realised, imparting a certain microwave-absorbing performance to the ZnO smoke. The research provides a new method for the comprehensive utilisation of zinc leach residue and the high-value utilisation of ZnO smoke [11-13].

2. Experimental work

2.1. Reagents and instruments

Zinc leach residue, CaO (analytically pure) and carbonaceous reducing agents (powdered coal) were used as main reagents in the experiment. The main equipment included an FA2104N electric balance, an alumina crucible, a KSL-1700X-A3 muffle furnace, a GJ-400-1 crusher, a FW-4 tablet press, and a DZF-6030A vacuum drying oven. The instruments, such as an Agilent 725 full-spectrum DC inductively coupled plasma atomic emission spectrometer, a D/max-2400 X-ray diffractometer, an XRF-1800 X-ray fluorescence spectrometer, a FEI Quanta 450 scanning electron microscope, a TECNAIG2 transmission electron microscope, and a PNA-N5244A vector network analyser (VNA) were used for analytical characterisations.

The X-ray fluorescence (XRF) spectra and full-spectrum DC inductively coupled plasma atomic emission spectra (ICP-AES) of zinc leach residue are summarised in Tables 1 and 2, respectively. Phase analysis results of zinc in the residue are listed in Table 3.

As seen from Table 1, zinc leach residue contains significant amounts of Fe_2O_3, SiO_2, SO_3, ZnO, and Na_2O, low amounts of valuable metals, and is of a complex composition. Loss on ignition is 8.13% at 450 °C.

Table 2 shows that 7.15% of zinc, 2.69% of lead, and 96.5 $g \cdot t^{-1}$ of silver are contained in zinc leach residue, showing high potential recovery value. As demonstrated in Table 3, zinc in the residue is mainly present in the forms of: $ZnFe_2O_4$, ZnO, Zn_2SiO_4, ZnS, and $ZnSO_4$ and is a mixed material with various regenerated compounds therein.

The results of XRD analysis of zinc leach residue are shown in Fig. 1: the main phase compositions of zinc leach residue contain: ZnS, SiO_2, Fe_2O_3, $KFe_3(SO_4)_2(OH)_6$, and $ZnFe_2O_4$.

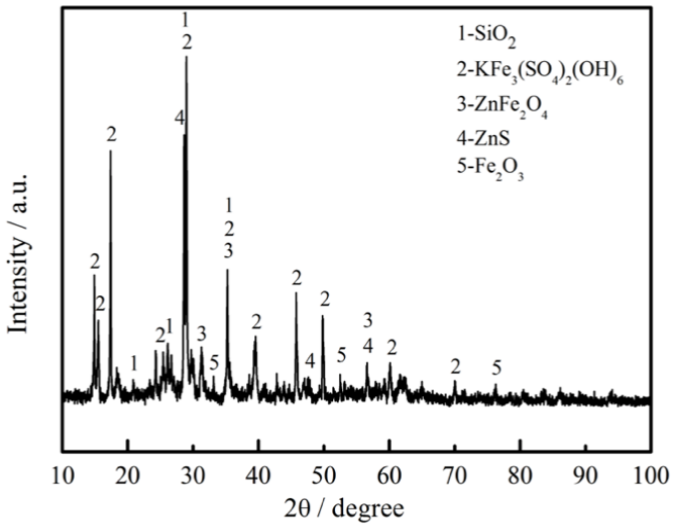

Fig. 1. XRD spectrum of zinc leach residue

TABLE 1

Results of XRF analysis of zinc leach residue (%, mass fraction)

Composition	Na_2O	MgO	Al_2O_3	SiO_2	SO_3	K_2O	CaO	TiO_2
Content	3.47	1.27	1.51	5.77	21.48	0.84	2.62	0.31
Composition	MnO	Fe_2O_3	CuO	ZnO	SrO	CdO	PbO	Loss on ignition
Content	1.54	34.06	0.19	5.16	0.20	5.04	0.52	8.13

TABLE 2

Results of ICP-AES analysis of zinc leach residue (%, mass fraction)

Element	Pb	Zn	TFe	Ca	S	Si	Al	Ag*
Content	2.69	7.15	20.3	1.18	11.75	4.42	0.76	96.5

Note: * Unit being $g \cdot t^{-1}$

TABLE 3

Phase analysis results of zinc (%, mass fraction)

Phase	ZnS	$ZnFe_2O_4$	Zn_2SiO_4	ZnO	$ZnSO_4$	Total
Content	0.96	3.90	0.45	1.23	0.61	7.15
Proportion	13.43	54.48	6.34	17.16	8.59	100

2.2. Experimental methods

The dried and crushed zinc leach residue was mixed with powdered coal and CaO in the mixing ratio of 10:5:1 and pressed into a cylinder with diameter of about 20 mm and height of 15 mm. After the muffle furnace was preheated to 1000°C, the cylinder was placed in a corundum crucible and then put in the muffle furnace. After separately heating to target temperatures (1200, 1250, and 1300°C), it was held for 60 min. Then the cylinder was cooled to room temperature in the furnace, and ZnO smoke and secondary slag were collected, weighed, characterised, and tested. Corresponding to different target temperatures, ZnO smoke samples were labelled S1, S2, and S3. The smoke generated during the experiment was emitted after alkali absorption.

3. Analysis and discussion of results

3.1. Chemical composition and microstructure of ZnO smoke

The chemical compositions and surface microstructures of smoke samples S1, S2, and S3 obtained from zinc leach residue at different temperatures were analysed by using the XRD, SEM, TEM, and STEM. Fig. 2 demonstrates XRD spectra of smoke from zinc leach residual treated by CTR at different temperatures: diffraction peaks of S1, S2, and S3 correspond to diffraction pattern of characteristic peaks of hexagonal ZnO (JCPDS card: 36-1451) and the peak intensity and peak position are consistent, without other impurity peaks. This indicates that ZnO generated by CTR of zinc leach residue has good crystallinity. Peak positions of S1, S2, and S3 at 31.77°, 34.42°, 36.25°, 47.54°, 56.60°, 62.86°, 67.96°, 92.78°, and 95.30° separately represent (100), (002), (101), (102), (110), (103), (112), (203), and (211) crystal faces, consistent results published elsewhere [14]. However, it is worth noting that, when diffraction peaks are found between

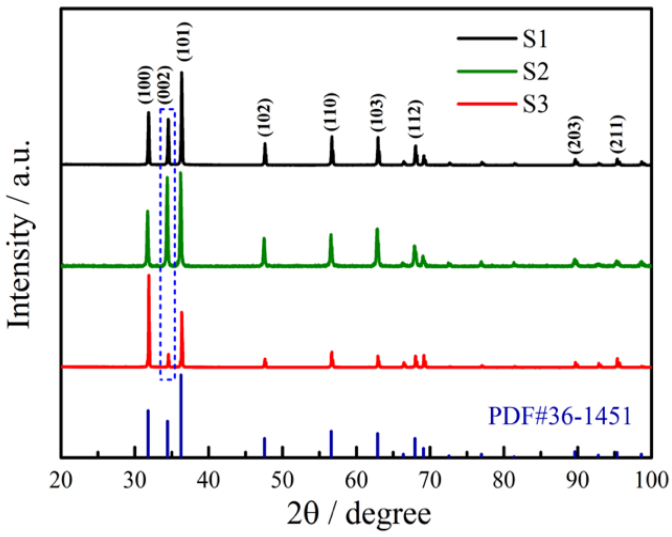

Fig. 2. XRD spectra of ZnO smoke

30° and 40°, the (100), (002), and (101) crystal faces of S1, S2, and S3 exhibit differences in crystallinity. Particularly, at 34.42°, the diffracted intensity of S2 along the (002) crystal face is the highest, suggesting (002) as the preferred orientation for growth.

TABLE 4

Average grain size calculated by X-ray diffraction peak data (30° to 65°)

Sample	Average grain size (nm)
S1	90.9
S2	61.3
S3	130.9

The grain size is calculated using Scherrer equation [15]:

$$D = 0.94\lambda/\beta\cos\theta \quad (1)$$

where D represents the average grain size (nm), λ denotes the wavelength of the incident X-ray, β is the width of the largest diffraction peak at 2θ, and θ represents the diffraction angle. It can be seen from Table 4 that S2 has the minimum average grain size, which is only 61.3 nm. The average grain sizes of S1 and S3 are 90.9 nm and 130.9 nm, respectively.

Fig. 3 shows SEM images of ZnO smoke from zinc leach residue by CTR at different temperatures: S1 and S3 are aggregated to a significant extent and have similar microstructures, with lamellar and island-like polymers therein. There are pores with different sizes ranging from dozens of nanometres to a few microns, without obvious particles therein. S2 is prismatic and rod-shaped, and the boundary of the micron-sized particles can be clearly seen. The comparison of microstructures of S1, S2, and S3 suggests that S2 has the smallest grain size, which matches the average grain size of ZnO calculated using the Scherrer equation. This indicates that the reaction environment at 1250°C is conducive to the rapid formation of the (002) crystal face of ZnO particles. Vapour deposition is a process in which crystal nucleation and crystal growth compete. Temperature plays a key role in crystal nucleation and growth and mainly controls the steam partial pressure of the system [16-18]. If the temperature is too low, the degree of supersaturation of reactants in the reaction system is too low, so that ZnO cannot nucleate and grow. With the increase of temperature, crystal nucleation and growth in the reaction system tend to be in dynamic equilibrium. When the temperature reaches a certain level, crystal growth dominates, growing preferentially in a certain orientation. At 1200°C, although the temperature is high enough, the microstructures of ZnO crystals are non-ideal, which means that the degree of supersaturation of ZnO in the system is low and the rate of crystal growth exceeds the rate of nucleation, thus generating non-granular island-like polymers. At 1250°C, crystal nucleation and crystal growth reach a relatively balanced state and ZnO tends to grow in spherical and rod-like forms. Too high a temperature can accelerate the rate of nucleation: in that case, the saturated vapour pressure of Zn is too high and the disordered gas phases can be rapidly deposited on the crystal

surfaces, so that the particles are bonded into laminates due to hard agglomerates.

Fig. 4 illustrates the mapping images of ZnO smoke S2: it appears as micron-sized ZnO particles, in which the ZnO content reaches 99.02%, approximate to the results of chemical analysis.

The TEM image of ZnO smoke obtained through CTR of zinc leach residue at 1250°C is shown in Fig. 5. The selected area electron diffraction pattern (SADP) was obtained and salient indices calibrated. By using Digital Micrograph software, electron diffraction spots obtained through Fourier transform of high-resolution diffraction fringes were compared with the standard PDF card of ZnO utilising spacing and angles between crystal faces as measured. This suggests that ZnO belongs to a hexagonal system and contains indices of (001), (00$\bar{1}$), (100), ($\bar{1}$00), (101), ($\bar{1}$0$\bar{1}$), (10$\bar{1}$), and ($\bar{1}$01) crystal faces. The calibration of electron diffraction spots confirms the existence of ZnO and the results coincide with XRD spectral data.

Fig. 6 shows STEM image and mapping images of elements of a single particle in the ZnO smoke from zinc leach residue treated by CTR at 1250°C: ZnO particles, after centripetal dispersion are about 0.6 μm in diameter and show cubic microstructures. Figs 6(b) and 6(c) demonstrate that Zn and O elements are evenly distributed on the surface of particles, in which the ZnO content reaches 99.44%.

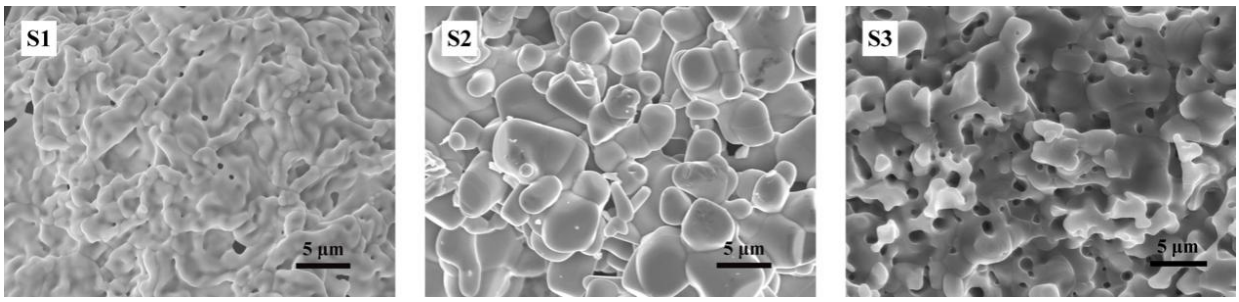

Fig. 3. SEM images of ZnO smoke obtained by CTR at different temperatures

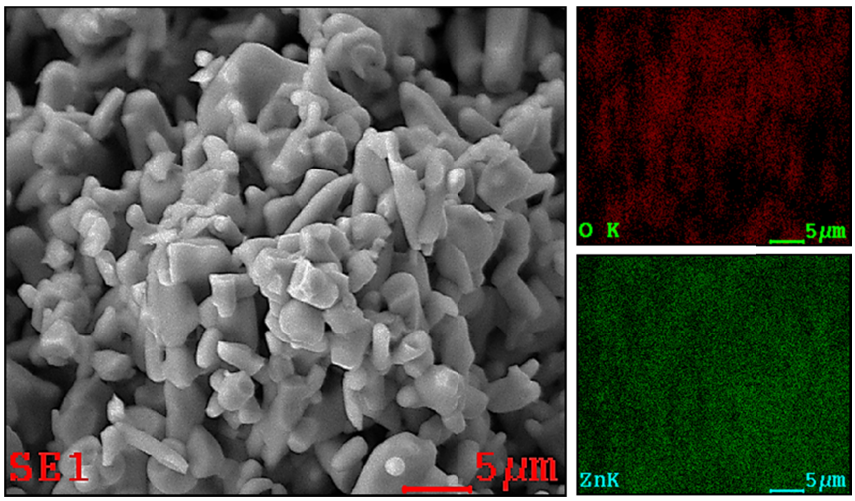

Fig. 4. Mapping images of ZnO smoke S2

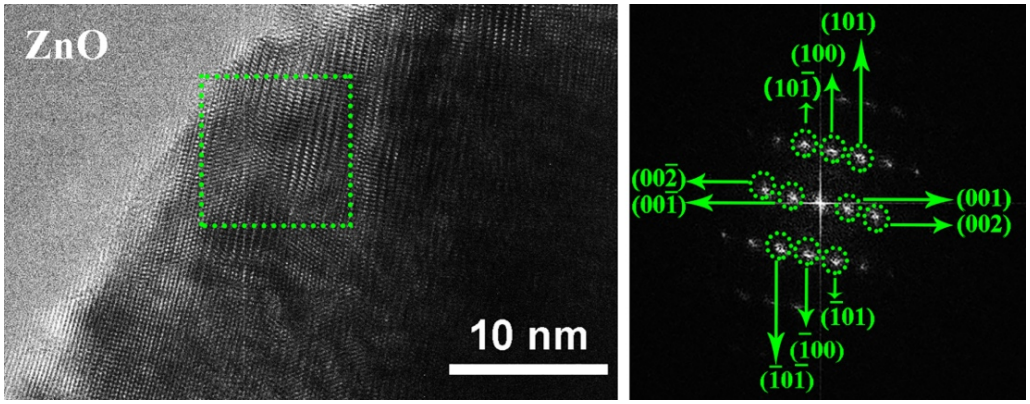

Fig. 5. TEM images of ZnO smoke obtained by CTR at 1250°C

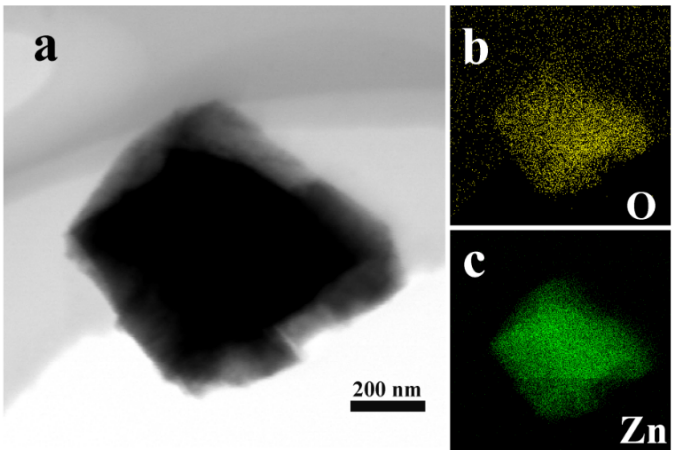

Fig. 6. STEM images of mapping images of ZnO smoke obtained by CTR at 1250°C

3.2. Microwave-absorbing properties of ZnO smoke

The volatilisation rate of zinc from the zinc leach residue was 97.31% and the ZnO content in the smoke was 99.14% under conditions involving calcinating the residue at 1250°C, holding for 60 min, and adding 50% carbon (powdered coal) and 10% CaO. To study microwave-absorbing properties of ZnO smoke, S1, S2, and S3 were mixed with molten paraffin at a mass ratio of 7.5:2.5 and then their electromagnetic parameters in the frequency range of 2 to 18 GHz were tested through the VNA. Complex dielectric constant and complex permeability are key to determination of the microwave-absorbing properties of the absorbers [19]. The real parts of complex dielectric constant (ε') and complex permeability (μ') represent storage capacities of electric and magnetic energy, while the imaginary parts (ε'' and μ'') describe loss capacities of electric and magnetic energy. Fig. 7 illustrates the relationships of complex dielectric constant ($\varepsilon_r = \varepsilon' - j\varepsilon''$) and complex permeability ($\mu_r = \mu' - j\mu''$) of ZnO smoke S1, S2, and S3 with frequency in the frequency range of 2 to 18 GHz.

As shown in Fig. 7(a), within the frequency range of 2 to 18 GHz, ε' of S2 is always higher than those of S1 and S3 and decreases with increasing frequency on the whole. Moreover, it slightly fluctuates after reducing from 9.35 to the minimum value (8.38). ε' of S1 shows a slight fluctuation after decreasing from 5.15 to the minimum value of 4.20, while that of S3 fluctuates between 4.20 and 3.81. It can be seen from Fig. 7(b) that ε'' of S2 presents a wave-like increasing trend with the constant increase of frequency and gradually rises from 1.02 to 1.95, while that of S1 shows a wave-like decreasing trend with continuously increasing frequency. Furthermore, ε'' of S3 fluctuates around 0.4. Fig. 7(c) and 7(d) illustrate that the change ranges of real and imaginary parts of complex permeabilities of S1 and S2 are small. μ' and μ'' separately fluctuate around 1 and 0 with changing frequency and the fluctuations can be deemed negligible. This indicates that microwave-absorbing properties of ZnO smoke S1, S2, and S3 are mainly determined by dielectric loss.

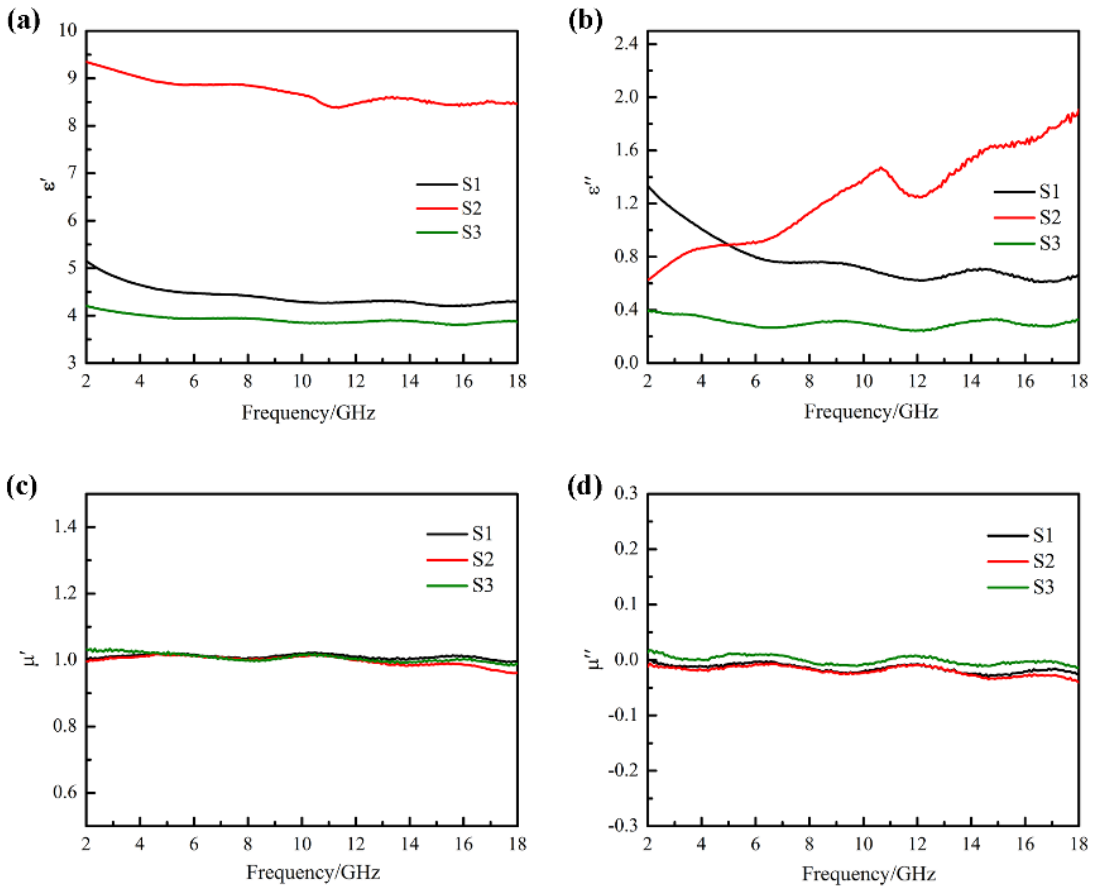

Fig. 7. The relationships between electromagnetic parameters of ZnO smoke and frequency

Based on complex dielectric constant and complex permeability, *RL* properties of ZnO smoke can be derived according to the theory of transmission lines and RL is an important parameter reflecting microwave-absorbing properties of the materials, as given by [20,21]:

$$RL = 20\lg\left|\frac{Z_{in}-1}{Z_{in}+1}\right|$$

where, Z_{in} represents the normalised input impedance of the materials in the free space and can be expressed as follows:

$$Z_{in} = \sqrt{\frac{\mu_r}{\varepsilon_r}}\tan h\left[j\left(\frac{2\pi fd}{c}\right)\sqrt{\mu_r\varepsilon_r}\right]$$

where, ε_r and η_r denote the complex dielectric constant and complex permeability of the materials, respectively; f denotes the frequency of electromagnetic waves; d and c separately indicate the thickness of microwave-absorbing materials and the propagation velocity of electromagnetic waves in vacuum.

Microwave-absorbing materials must be light, thin (when used as coatings), of a wide frequency band, offering strong microwave-absorption [22]. Fig. 8 compares *RL* properties of ZnO smoke specimens S1(a), S2(b), and S3(c) calculated within the frequency range of 2 to 18 GHz. The thickness (D) of the absorbers varies from 1 mm to 5 mm and, with the increase of the thickness of the samples, RL peaks of the samples of ZnO smokes S1 and S3 gradually shift from a high frequency to a low frequency, while the minimum reflection loss (RL_{min}) of S2 is lower than those of S1 and S3. In Figs 8(a) and (c), RL_{min} of sample S1 at a frequency of 8 GHz is –5.23 dB and its matching thickness is 5 mm, while RL_{min} of sample S3 is only –2.46 dB at 15.12 GHz and its matching thickness is 3 mm. In Fig. 8(b), at 17.84 GHz, RL_{min} of sample S2 can reach –20.18 dB and its matching thickness is 4.5 mm. In addition, RL_{min} of the sample reaches -25.56 dB at 15.84 GHz and its matching thickness is 5 mm. Moreover, the bandwith corresponding to $RL < -10$ dB is 2.0 GHz. Under each of the matching thicknesses of 4.5 and 5 mm, two *RL* peaks appear for sample S2 and the distance between them constantly decreases as a result of destructive interference of waves. According to calculation using the Scherrer equation, it was found that sample S2 has the minimum grain size, so particles therein have more interfaces per unit volume than S1 and S3. As a result, S2 presents stronger interfacial polarisation than S1 and S3, so it has a better microwave-absorbing performance. Moreover, as S2 has a preferred orientation along the (002) crystal face, anisotropy of S2 crystals differs from that of S1 and S3, which leads to S2 having different dielectric properties to S1 and S3.

The further to investigate various mechanisms of dielectric loss in ZnO smoke S2, the $\varepsilon'' - \varepsilon'$ curves are plotted (Fig. 9). In accordance with Debye's theorem [23], a relaxation process generally corresponds to a semicircle (the so-called Cole-Cole semicircle). It can be seen from Fig. 9 that three Cole-Cole semicircles appear in S1, S2, and S3. This means that ZnO smoke undergoes a process of dielectric relaxation at high frequency, which is conducive to improving the absorption properties of electromagnetic waves by the samples.

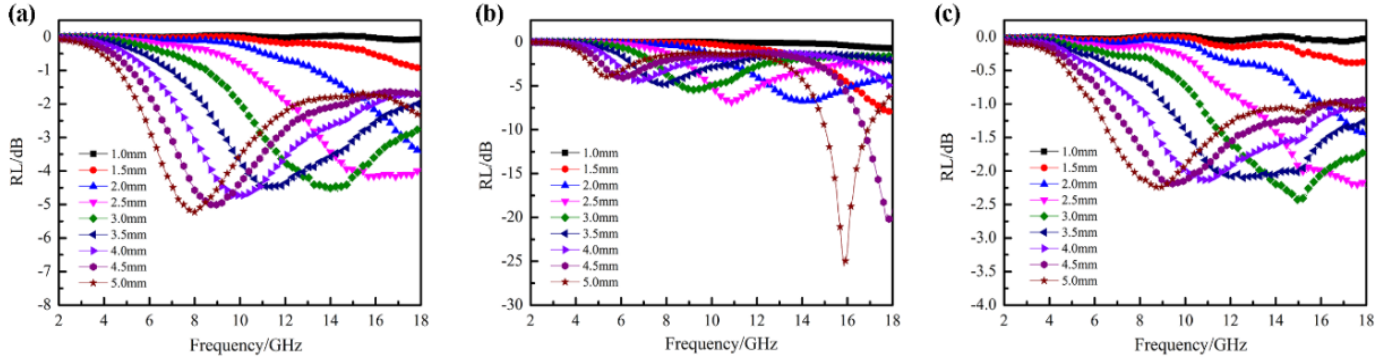

Fig. 8. The relationship between RL of ZnO smoke and frequency

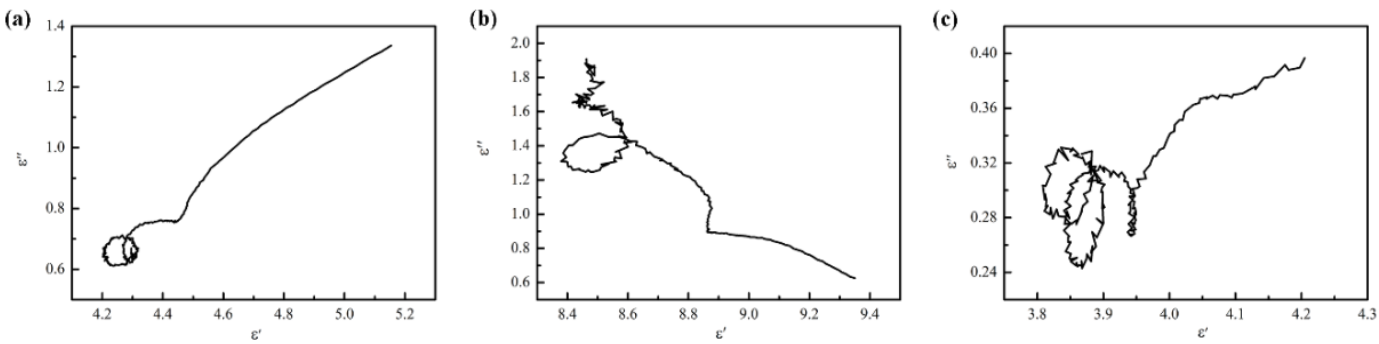

Fig. 9. Cole-Cole curves of ZnO smoke samples S1(a), S2(b), and S3(c)

4. Conclusion

Based on CTR, ZnO smoke obtained separately at reaction temperatures of 1200, 1250, and 1300°C, holding for 60 min, and adding 50% and 10% powdered coal and CaO, respectively, has large differences in microstructure. ZnO smoke at 1250°C presents a preferred orientation along the (002) crystal face and microscopically forms micron-sized particles with rod-like and spherical structures. The analysis of the microwave-absorbing properties of ZnO smoke at different temperatures demonstrate that such properties of ZnO smoke are mainly brought about by dielectric loss and are optimal at 1250°C. RL_{min} reaches –25.56 dB at a frequency of 15.84 GHz and its matching thickness is 5 mm. The bandwidth corresponding to $RL < -10$ dB is 2.0 GHz (14.90 GHz to 16.90 GHz). In future work, enrichment and separation of the metals in waste residue should be further studied from the perspectives of industrialised and high-value production of zinc leach residue. This study provides a new idea for high-efficiency, high-value utilisation of zinc leach residue.

Supplementary materials: Thermodynamic Analysis

The possible reaction of zinc and its compounds in the carbothermal reaction of zinc leach residue is shown in formula (1)-(10). The relationship between the standard Gibbs free energy of reaction (1)-(10) and temperature calculated by reaction plate in Factpage 7.3 is shown in Fig. A1 and Fig. A2.

$$3ZnFe_2O_4 + CO = 3ZnO + 2Fe_3O_4 + CO_2 \quad (1)$$

$$ZnFe_2O_4 + CO = ZnO + 2FeO + CO_2 \quad (2)$$

$$ZnFe_2O_4 + FeO = ZnO + Fe_3O_4 \quad (3)$$

$$Fe_3O_4 + CO = 3FeO + CO_2 \quad (4)$$

$$ZnS + CaO + C = Zn(g) + CaS + CO \quad (5)$$

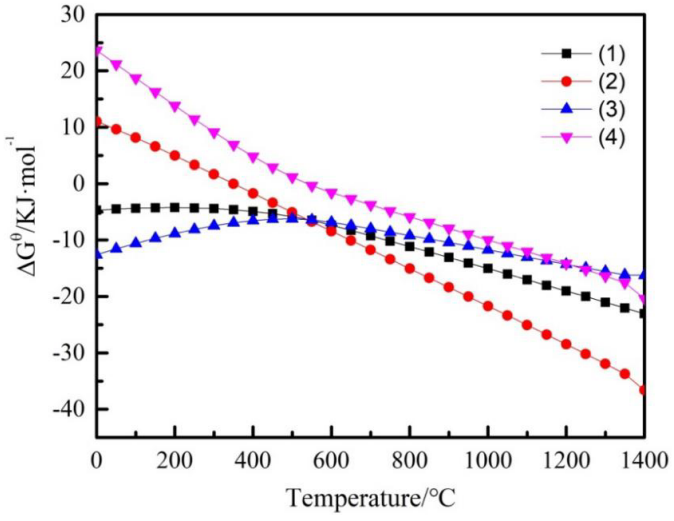

Fig. A1. The relationship between Gibbs free energy and temperature

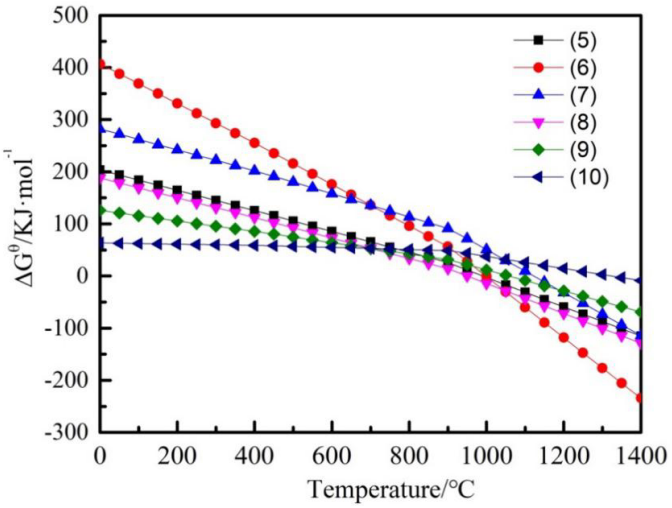

Fig. A2. The relationship between Gibbs free energy and temperature

$$Zn_2SiO_4 + 2C = 2Zn(g) + SiO_2 + 2CO \quad (6)$$

$$Zn_2SiO_4 + 2CO = 2Zn(g) + SiO_2 + 2CO_2 \quad (7)$$

$$ZnO + C = Zn(g) + CO \quad (8)$$

$$2ZnO + C = 2Zn(g) + CO_2 \quad (9)$$

$$ZnO + CO = Zn(g) + CO_2 \quad (10)$$

It can be seen from Fig. A1 and Fig. A2 that the zinc compounds in the zinc leaching residue are reduced to ZnO in the process of carbothermal reduction (1,100°C ~ 1,350°C), ZnO is further reduced to zinc vapor, the gaseous zinc is oxidized to ZnO as the furnace gas rises, and finally collected in the form of ZnO fume.

Acknowledgment

This work was supported by the Joint Fund between Shenyang National Laboratory for Materials Science and The State Key Laboratory for Advanced Processing and Recycling of Non-ferrous Metals for "One-step harmless treatment of zinc and silver-rich residue using the smelting–volatilisation method" (Grant no. 18LHZD001), The Department of Industry and Information Technology of Gansu Province for a "Technical study on the harmless treatment of zinc and silver-rich residue using the fuming process" (Grant no. GGLD-2019-046), and a Gansu Major Science and Technology Project for "Development and industrialisation of key technologies for enrichment of rare metals in zinc hydrometallurgy" (Grant no. 19ZD2GD001).

REFERENCES

[1] M. Li, B. Peng, L.Y. Chai, Technological Mineralogy and Environmental Activity of Zinc Leaching Residue from Zinc Hydrometallurgical Process, T. Nonfer. Metal. Soc. **23** (5), 1480-1488 (2013). DOI: https://doi.org/10.1016/S1003-6326(13)62620-5

[2] G.M. Jiang, B. Peng, Y.J. Liang, Recovery of Valuable Metals from Zinc Leaching Residue by Sulfate Roasting and Water Leaching, T. Nonfer. Metal. Soc. **27**, 1180-1187 (2017). DOI: https://doi.org/10.1016/S1003-6326(17)60138-9

[3] H. Yan, L.Y. Chai, B. Peng, A Novel Method to Recover Zinc and Iron from Zinc Leaching Residue, Mine Eng. **55**, 103-110 (2014). DOI: https://doi.org/10.1016/j.mineng.2013.09.015

[4] W. Luo, Q. Feng, L. Ou, Kinetics of Saprolitic Laterite Leaching by Sulphuric Acid at Atmospheric Pressure, Mine Eng. **23** (6), 458-462 (2010). DOI: https://doi.org/10.1016/j.mineng.2009.10.006

[5] L. Tang, C.B. Tang, J. Xiao, A Cleaner Process for Lead Recovery from Lead-containing Hazardous Solid Waste and Zinc Leaching Residue Via Reducing-matting Smelting, J. Clean Prod. **241**, 1-8 (2019). DOI: https://doi.org/10.1016/j.jclepro.2019.118328

[6] A. Özverdi, M. Erdem, Environmental Risk Assessment and Stabilization/Solidification of Zinc Extraction Residue: I. Environmental Risk Assessment, Hydrometallurgy **100**, 103-109 (2010). DOI: https://doi.org/10.1016/j.hydromet.2009.10.011

[7] J.M. Steer, A.J. Giffiths, Investigation of Carboxylic Acids and Non-aqueous Solvents for the Selective Leaching of Zinc from Blast Furnace Dust Slurry, Hydrometallurgy **140**, 34-4 1(2013). DOI: https://doi.org/10.1016/j.hydromet.2013.08.011

[8] P. Xing, B.Z. Ma, P. Zeng, Deep Cleaning of a Metallurgical Zinc Leaching Residue and Recovery of Valuable Metals, Int. J. Min. Met. Mater. **24** (11), 1217-1227 (2017). DOI: https://doi.org/10.1007/s12613-017-1514-2

[9] S. Wang, Y.Y. Shen, S.Q. Zhang. Leaching of High Arsenic Content Dust and a New Process for the Preparation of Copper Arsenate, Arch. Metall. Mater. **63** (3), 1167-1172 (2018). DOI: https://doi.org/10.24425/123789

[10] X.B. Li, C. Wei, Z.G. Deng, Extraction and Separation of Indium and Copper from Zinc Residue Leach Liquor by Solvent Extraction, Sep. Purif. Technol. **156**, 348-355 (2015). DOI: https://doi.org/10.1006/j.seppur.2015.10.021

[11] O.N. Kononova, A.G. Kholmogorov, N.V. Danilenko, Recovery of Silver from Thiosulfate and Thiocyanante Leach Solutions by Adsorption on Anion Exchange Resins and Activated Carbon, Hydrometallurgy **88**, 189-195 (2007). DOI: https://doi.org/10.1016/j.hydromet.2017.03.012

[12] G.G. Mei, D.R. Wang, J.Y. Zhou, Zinc Hydrometallurgy [M], Central South University of Technology Press, 2001 China, Changsha.

[13] G. Yu, N. Peng, L. Zhou, Selective Reduction Process of Zinc Ferrite and its Application in Treatment of Zinc Leaching Residues. T. Nonfer. Metal. Soc. **55**, 103-110 (2014). DOI: https://doi.org/10.1016/S1003-6326(15)63899-7

[14] I. M. Alibe, K.A. Matori, H.A.A. Sidek, The Influence of Calcination Temperature on Structural and Optical Properties of ZnO-SiO2 Nanocomposite by Simple Thermal Treatment Route, Arch. Metall. Mater. **63** (2), 539-545 (2018). DOI: https://doi.org/10.24425/118972

[15] M.H. Tang, M.Z. Chen, X. Zhu, Elimination of 180° Non-uniqueness of ZnO Diffraction Pattern, Anal. Test. Technol. Instrum. **23** (2), 130-134 (2017). DOI: https://doi.org/10.16495/j.1006-3757.2017.02.012

[16] G.Z. Liu, Z.D. Wang, Z.G. Wan, Study on Microwave Synthesis of ZnO Microrods, J. Hubei. Univ. Technol. **22** (5), 5-7 (2007).

[17] I.M. Alibe, K.A. Matori, E. Saion, The Influence of Calcination Temperature on Structural and Pptical Properties of ZnO Nanoparticles Via Simple Polymer Synthesis Route, Sci. Sinter. **49** (3), 263-275 (2017). DOI: https://doi.org/10.2298/SOS1703263A

[18] I.M. Alibe, K.A. Matori, H.A.A. Sidek, Effects of Calcination Holding Time on Properties of Wide Band Gap Willemite Semiconductor Nanoparticles by the Polymer Thermal Treatment Method, Molecules **23** (4), 1-18 (2018). DOI: https://doi.org/10.3390/molecules23040873

[19] S. Geetha, K.K.K. Satheesh, C.R.K. Rao, EMI Shielding: Methods and Materials. A Review. J. Appl. Polym. Sci. **112** (4), 2073-2086 (2010). DOI: https://doi.org/10.1002/app.29812

[20] L.L. Yan, M. Zhang, S.C. Zhao, Wire-in-tube ZnO@carbon by Molecular Layer Deposition: Accurately Tunable Electromagnetic Parameters and Remarkable Wave Absorption, Chem. Eng. J. **382**, 1-11 (2020). DOI: https://doi.org/10.1016/j.cej.2019.122860

[21] X. Meng, Y.Q. Liu, G.H. Han, Three-dimensional (Fe3O4/ZnO)@C Double-core@shell Porous Nanocomposites with Enhanced Broadband Wave Absorption, Carbon **162**, 356-364 (2020). DOI: https://doi.org/10.1016/j.carbon.2020.02.035

[22] L.Z. Zhao, S.X. Hu, S.W. Li, Absorption Principle and Research Progress of Absorbing Materials, Modern Defense. Technol. **35** (1), 27-31 (2007).

[23] X.J. Zhang, G.S. Wang, Y.Z. Wei, Polymer-composite with High Dielectric Constant and Enhanced Absorption Properties Based on Grapheme-CuS Nanocomposites and Polyvinylidene Fluoride, J. Mater. Chem. A **1** (39), 12115-12122 (2013). DOI: https://doi.org/10.1039/c3ta12451g